Nearfield Vortex Dynamics of Supercell Bloch Modes

Xiaona Ye,[1,*] Guangfeng Wang,[1,*] Xiaoyang Duan,[2,†] Ziwei Wang,[1] Zengya Li,[1] Tongtong Jia,[3] Tingxin Li,[3] Luqi Yuan,[1] Bo Wang,[1,‡] and Xianfeng Chen[1,4,5,§]

[1]*State Key Laboratory of Photonics and Communications, School of Physics and Astronomy, Shanghai Jiao Tong University, Shanghai 200240, China*

[2]*State Key Laboratory of Chips and Systems for Advanced Light Field Display, Key Lab of advanced optoelectronic quantum architecture and measurement (Ministry of Education), School of Physics, Beijing Institute of Technology, Beijing 100081, China*

[3]*Key Laboratory of Artificial Structures and Quantum Control (Ministry of Education), School of Physics and Astronomy, Shanghai Jiao Tong University, Shanghai 200240, China*

[4]*Shanghai Research Center for Quantum Sciences, Shanghai 201315, China*

[5]*Collaborative Innovation Center of Light Manipulations and Applications, Shandong Normal University, Jinan 250358, China*

(Received 13 November 2024; revised 16 March 2025; accepted 13 May 2025; published 17 June 2025)

Densely arranged optical vortices are natural solutions of high-symmetry Bloch modes in photonic crystals. However, strict symmetry constraints limit the potential spatial configurations of nearfield vortices, restricting the control over light-matter interaction. Here, we demonstrate a nearfield vortex dynamic within a supercell photonic crystal. By introducing paired rotations of triangular structures, we achieve high-quality-factor Bloch mode transition from evanescent valley modes, to quasibound states in the continuum, frustrated modes, and quasivalleys. Each stage exhibits distinct nearfield vortex distributions, nonlinear overlap properties, and quality factors, revealing diverse physical behaviors for tailoring light-matter interaction. Notably, the asymmetric vortex configuration of frustrated modes enhances second harmonic generation, driven by an optimized nonlinear overlap factor. Our paired-rotation strategy offers a versatile design framework for creating supercell photonic crystals with unique nearfield vortex properties, presenting promising applications in lasing, nonlinear optics and optical forces.

DOI: 10.1103/svcj-vgzw

Introduction—The strong light-matter interaction achieved from high-quality (Q) factor Bloch modes of photonic crystal slabs (PCSs) can boost many optical effects within a subwavelength thickness, with many applications in laser [1,2], single photon generation [3], and high-order harmonic generation [4–6]. The exploiting of group theory and parameter perturbation method has provided a paradigm for designing novel PCSs [7–9]. Multiple design approaches, including BIC merging [10], Brillion-zone folding [11], twisted or Moiré PCSs [12–15], and engineered rotational symmetry [16,17], have been proposed to enrich the parameter space for designing PCSs with different functionalities. In particular, the rotation of geometry structures has shown as a powerful means to flexibly tune the optical properties of PCSs. For instance, the slightly rotating of structures can break C_2 symmetry, inducing quasibound states in the continuum (BICs) [18,19]. For honeycomb PCSs, the rotation of C_3 structure will open the Dirac point to form topological valley pairs [20,21]. Moreover, spatially varying rotation of C_2 structures gives rise to real-space geometric phases for customized laser radiation [22–24].

A particular case of utilizing PCSs for enhanced light-matter interaction is to generate second harmonic (SH), which is usually a very weak effect that requires a sufficiently long accumulation distance to obtain a fair conversion efficiency. For PCSs and other optical structures of a similar thickness [25–30], the SH accumulation is achieved by enhanced Q factor. Notably, the asymmetric nature of SH generation also requires a strong nonlinear field overlapping (β) between the fundamental mode and SH mode [31]. However, optical structures with symmetry-guaranteed high-Q modes usually result in very small β [32]. For instance, the extremely high-Q factor of quasi-BICs (qBICs) emerges from structures with a C_{2n} symmetry, while a considerably large β arises from those with a C_{2n+1} symmetry [33–35]. This $Q-\beta$ contradiction has become a main barrier that hinders us to find an optimized solution for SH generation in PCSs and metasurfaces. Therefore, seeking a balance between spatial symmetry breaking and high-Q effect are critical for optimized SH generation in resonate structures, which requires novel design strategies beyond conventional photonic devices. Recently,

*These authors contributed equally to this work.
†Contact author: xduan@bit.edu.cn
‡Contact author: wangbo89@sjtu.edu.cn
§Contact author: xfchen@sjtu.edu.cn

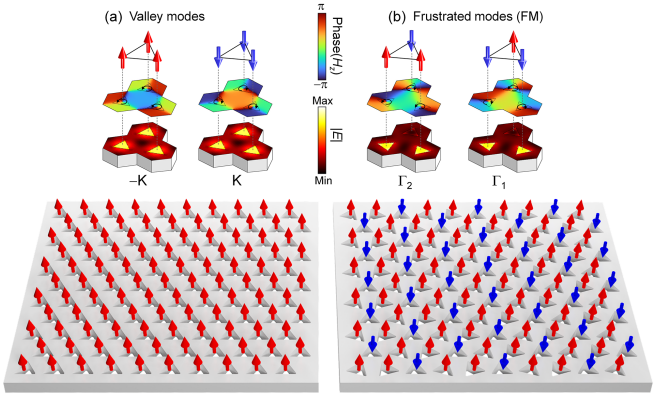

FIG. 1. Concept illustration of frustrated photonic Bloch modes. (a) The ±K-valley modes of a conventional PCS consisting of a hexagonal array of triangular meta-atoms. (b) Degenerate frustrated modes in a supercell PCS. The arrows represent pseudospin vectors defined by the local phase vortices at the centers of triangular meta-atoms.

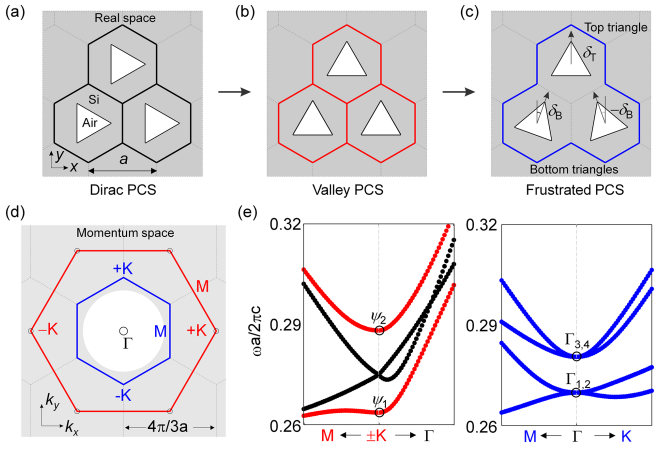

FIG. 2. Supercell PCS and corresponding band structures. (a), (b) Structures of conventional PCSs consisting of triangular meta-atoms with uniform rotation angles of $\delta = \pi/6$ (Dirac) and $\delta = 0$ (Valley), respectively. (c) Designed structure of a frustrated supercell PCS. The angle of the top triangular meta-atom is $\delta_T = 0$, and the angles of the bottom triangles are $\pm\delta_B$. (d) Brillouin zones for the valley PCS (red hexagon) and the supercell PCS (blue hexagon). The shaded area represents the waveguide region. (e) TE band structure of the Dirac or valley PCSs (red and black dots) around ±K points and the supercell PCSs (blue dots) around Γ point.

diversity approaches have been introduced to increase the overlapping factor for SH generation [36–42], such as by designing doubly resonant structures [37,41], and inversely engineered modes [40], or by controlling the SH radiation pattern [36] and material's nonlinear susceptibility [38,39].

In this work, we designed a C_3 supercell PCS and observed unique nearfield vortex dynamics. The supercell PCS features three triangular meta-atoms arranged in a hexagonal lattice, with a pair of opposite rotations of the bottom triangles tuning the in-plane rotational symmetry and valley mode coupling. As the bottom triangles rotate, three free vortices in the supercell move towards the top triangle. During this process, distinct Bloch modes are revealed from different vortex distributions. Four typical stages are valley modes, qBICs, frustrated modes (FMs), and quasivalleys (qValleys). These Bloch modes are characterized by different nearfield vortex formation, quality factor, field asymmetry, and even energy flow, providing a very rich realm to modulate light-matter interactions by simply rotating the unitcell structures. In particular, there is a critical point where four vortices are merged, forming degenerate "two-down–one-up" and "two-up–one-down" frustrationlike states [Fig. 1(b)], with "up" or "down" being the handedness of the phase vortex. This pseudospin feature is an optical analogy to geometric frustration, which exhibits similar asymmetric spin (magnetic) configuration [43]. The FM is associated with a maximum β from its unique asymmetric vortex formation. Meanwhile, the radiative Q factor reaches a minimum, corresponding to a positive topological charge in the parameter space. The vortex distribution in the supercell has guaranteed a considerably large $Q\beta$, making the FM as an optimized solution for SH generation.

Bloch mode dynamics in the supercell PCS—We start the theoretical analysis by examining the transverse electric modes of a PCS consisting of a hexagonal lattice of triangular meta-atoms [Figs. 2(a) and 2(b)]. Initially, the triangles are uniformly rotated from the y axis by an angle δ, which determines the PCS's symmetry and band degeneracy. Specifically, for $\delta = (2m+1)\pi/6$ $(m \in \mathbf{Z})$, the point group at the corners (±K) of the Brillouin zone exhibits C_{3v} symmetry, corresponding to double-degenerate Dirac modes [Fig. 2(e), the black bands]. Otherwise, the symmetry reduces to C_3, and the twofold Dirac degeneracy is lifted to form a valley pair [ψ_1 and ψ_2 at ±K in Fig. 2(e)] [44–46].

Based on this δ-dependent valley PCS, we introduce a supercell structure composed of three neighboring unitcells [Fig. 2(c)]. In the supercell, the rotation angle of the top triangle is set as δ_T, while the bottom triangles are characterized by a pair of opposite angles, $\pm\delta_B$. This design strategy is inspired by a natural noncentrosymmetric compound HoAgGe, where the structural distortion is similarly characterized by opposite rotations of two types of triangles to induce frustration [47]. Two straightforward outcomes from the supercell PCS are (I) the reduction of the Brillion zone [Fig. 2(d)] and (II) band structure folding from the K points to Γ points with valley mode coupling [Fig. 2(e)]. Specifically, in the supercell structure, the valley pairs ψ_1 and ψ_2 become two pairs of modes, $\Gamma_{1,2}$ and $\Gamma_{3,4}$. Their eigenfrequencies are determined by δ_T and δ_B, which induces distinct valley mode coupling [Fig. 3(c)]. The double degeneracy will always remain due to the supercell C_3 symmetry.

As an example, we evaluated the Q-factor evolution of the $\Gamma_{1,2}$ mode via simultaneously rotating δ_T and δ_B.

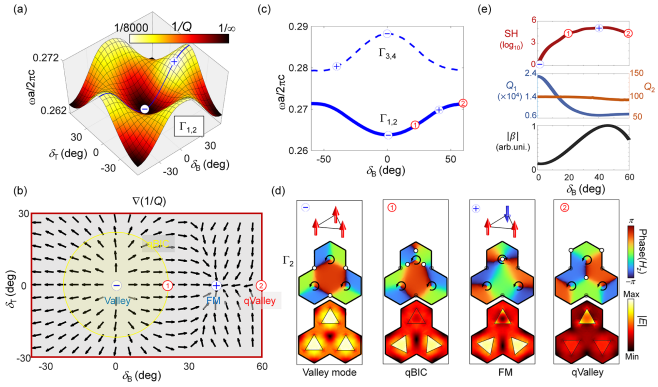

FIG. 3. Evolution of Bloch modes and SH enhancement in parameter space. (a) The dispersion surface of $\Gamma_{1,2}$ modes and the corresponding radiation loss $(1/Q)$ mapped in the parameter space (δ_T, δ_B). The "−" and "+" signs are locations with a minimal and maximal $1/Q$. (b) The vector map of $\nabla(1/Q)$ in the rotation parameter space. (c) The eigen frequency evolution of two pairs of Γ-point modes as a function of δ_B, for $\delta_T = 0°$. The dashed curve represents the higher pair of modes, $\Gamma_{3,4}$. (d) Selected pseudospin textures $\mathbf{S}$ (top panel), nearfield vortex distributions (middle panel), and electric field distributions (bottom panel) for four Γ_2 modes in corresponding to the marks in (c). The transparent black dots are the original locations of the free vortices starting from $\delta_B = 0$. (e) Simulated SH enhancement, Q (Q_1 for fundamental wave and Q_2 for SH) and $|\beta|$ as a function of δ_B, which is calculated by exciting the $\Gamma_{1,2}$ modes with a circularly polarized plane wave. These vortices are shown by decomposing the paired Bloch modes into a pair of opposite circularly polarized modes.

The radiative loss $(1/Q)$ of $\Gamma_{1,2}$ mode is shown in Fig. 3(a), with the minus and plus signs indicating two extreme points. In fact, for $\delta_T = \delta_B = 0$, the $\Gamma_{1,2}$ are K-point valley modes, which have an infinite Q factor as they are residing in the evanescent region. Any slight change of (δ_T, δ_B) around the valley mode will induce a sudden transition from valley modes to paired qBICs, resulting in a very high but finite Q factor. Therefore, the valley mode exhibits a negative topological charge $q = -1$, where the $\nabla(1/Q)$ vectors are diverging to form a negative singularity. The qBIC region is characterized by a quadratically decayed Q factor along with the rotational parameters, that is, $Q \propto (\delta_T^2 + \delta_B^2)^{-1}$. This qBIC region is approximately sketched by the circle in Fig. 3(b) [48] (details in Fig. S14). In contrast, a largest radiative loss occurs around $(\delta_T, \delta_B) = (0, 40°)$, corresponding to a positive topological charge $q = 1$, where the $\nabla(1/Q)$ vectors are converging and forming a positive singularity. This minimal Q factor is equivalent to a maximum of radiation loss, as $|\kappa| \propto 1/\sqrt{Q}$ [50]. This mode is also referred to as a FM—a unique vortex-merged Bloch state that will be explained later. Notably, the symmetry constraint of the supercell requires that the topological charge q can only occur for $\delta_T = m\pi/3$ [48] (Supplemental Material, Sec. S7). Therefore, there is only one pair of opposite topological charges in the (δ_T, δ_B) space [48] [see Fig. 3(b), and the $\nabla(1/Q)$ vectors across the entire parameter space is shown in Fig. S13 [48]].

A clear mode evolution can be visualized from the supercell vortex dynamic. Figure 3(d) shows several typical nearfield examples of Γ_1 with H_z phase vortices. The vortices of valley modes are periodically arranged in the PCS with an equal distance. One group of vortices reside at the centers of the triangles [Fig. 3(d) left panel, the circled arrows], while the other group of opposite vortices are located at three corners of the supercell boundaries [Fig. 3(d), the white dots]. We define the vortices at the centers of the triangles as pseudospin vectors, $\mathbf{S} = \pm\mathbf{z}$, with $\mathbf{z}$ being the direction of $\mathbf{S}$, corresponding to a clockwise or anticlockwise phase vortex, respectively. The vortices at the corners of the supercells are referred to as free vortices, as they will move in the nearfield once we change δ_B. Pseudospin vortices always remain at the center of the triangles, and they can be utilized to characterize valley index [23]. In contrast, as δ_B changes, free vortices move towards the top triangle with different displacements from their original locations, resulting in distinct Bloch states [48] (Supplemental Material, Sec. S8).

In term of vortex distribution, there are three other typical states besides valley modes. The qBICs are Bloch modes with their free vortices slightly deviated from that of the valley modes [Fig. 3(d), second panel]. The qValley mode occur for $\delta_B = 60°$, which exhibits the same vortex distribution with valley mode, but with a different spatial intensity periodicity [Fig. 3(d), fourth panel]. There is a critical point of δ_B, at which the free vortices are merged with the upper pseudospin, resulting in a FM with two-down–one-up or two-up–one-down supercell vortex formation, akin to a magnetic frustration. Here, up or down is defined by the sign of $\mathbf{S} = \pm\mathbf{z}$, respectively. The critical point $\delta_B \in (0°, 60°)$ is determined by the geometric parameters of the PCS. Notably, because of this unique vortex distribution in the supercell, FM is associated with the highest radiative loss $(q = 1)$ and a strong spatial asymmetry in the electric field distribution [the lower panel of Fig. 3(d)]. The symmetry constraint of the supercell also requires that the FM can only occur for $\delta_T = m\pi/3$ [48] (Supplemental Material, Sec. S7).

A potential application of the FM is SH enhancement from its spatial asymmetry. Experimentally, we achieved a 10^6 enhancement from a FM compared to a Si film, which does not generate SH from bulk material. Figure 3(e) shows the simulated results of SH enhancement, Q factors and $|\beta|$ on the $\Gamma_{1,2}$ band from on-resonant pumping with a circularly polarized plane wave. Notably, the highest SH enhancement occurs around FM, rather than qBICs (although they exhibit the highest finite Q factors). Based on temporal coupled-mode theory, we find that the FM mode has a maximum β associated with its unique vortex distribution [48] (Sec. S9). Moreover, Figs. 3(b) and 3(e) also show a strong SH generation in a wide δ_B range

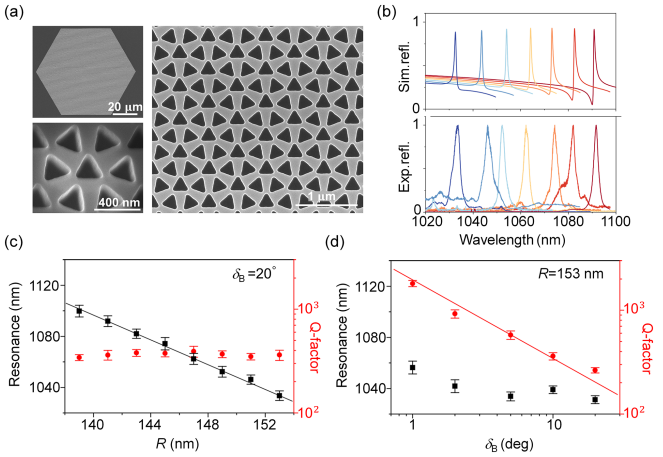

FIG. 4. Spectral characterization of supercell PCSs. (a) SEM images of a typical supercell PCS with $\delta_B = 20°$. (b) Simulated (upper panel) and measured (lower panel) reflectance spectra of the Si PCSs with various radii R. The R decreases from 153 to 141 nm in a step of 2 nm from the leftist to the rightest spectrum. The lattice constant is $a = 315$ nm and $\delta_B = 20°$. (c) Measured resonance wavelengths and Q factors for supercell PCSs with different R. (d) Measured resonance wavelengths and Q factors as a function of δ_B.

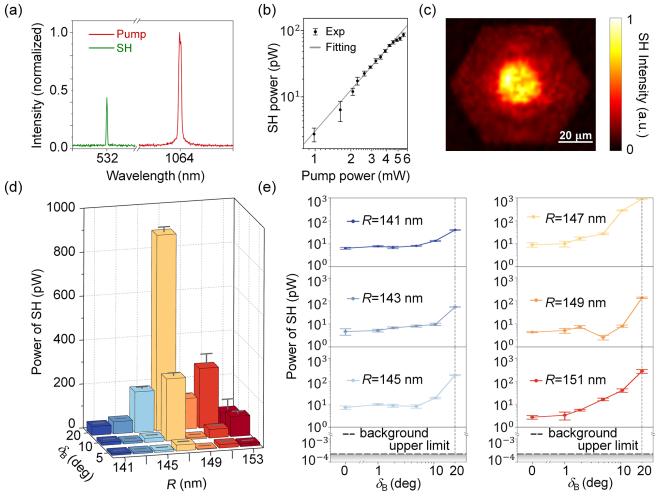

FIG. 5. Experimental characterization of the SH enhancement from supercell PCSs. (a) Typical spectrum of fundamental wave (red) and SH generation (green). (b) Power dependence of SH on a logarithmic scale, showing quadratic power scaling. The black dots represent the measured data, and the line is fitted with a second-order power function. (c) Measured SH by scanning the pumping laser over the surface of a supercell PCS for $R = 147$ nm and $\delta_B = 20°$. This intensity distribution indicates the spatial profile of the Bloch modes from the PCS. (d) Measured SH power as a function of R and δ_B from a circularly polarized pump beam with a power of 14.3 mW. (e) Selected experimental SH generation as functions of δ_B. The background upper limit (horizontal dashed lines) is the SH signal measured from Si film, which is ~6 orders of magnitudes smaller than the maximum SH enhancement from the PCSs.

around the FM, indicating a robust performance against the rotation of triangles. An important criterion is that the SH increases as δ_B changes from 0° to 20°, then the SH generation becomes stable.

Experimental characterization of supercell PCS enhanced SHG—Experimentally, we fabricated a series of PCSs with varying geometric parameters using a silicon-on-insulator device [48] (Supplemental Material, Sec. S1). The thickness of the silicon film is $H = 220$ nm. The lattice constant of the PCS is $a = 315$ nm, and the circumcircle radius R of the triangles ranges from 141 nm to 153 nm, with several δ_B selectively chosen from 0 to 20° [48] (Supplemental Material, Sec. S5). Typical scanning electron microscope images are shown in Fig. 4(a) for the case of $\delta_B = 20°$. We used a cross-polarized reflectance spectral characterization to measure the spectra of different PCSs [Fig. 4(b)], which are in good agreement with the simulations. Moreover, the wavelength of the resonant mode and Q factors are systematically characterized by measuring different PCSs with varying R and δ_B [Figs. 4(c) and 4(d)]. Particularly, the change of δ_B from 0° to 20° will reduce the Q factor from ~2000 to ~200, indicating a mode transition from valley, via qBICs, towards FM.

We experimentally characterized the SH of the supercell PCSs using a pulsed laser (~8 ps) with a central wavelength of 1064 nm and a repetition rate of 20 MHz. The pump light is circularly polarized with a focused spot size of ~2 μm, impinging onto the PCSs with a normal incident angle [48] (Supplemental Material, Sec. S3). Typical spectra for the pump laser and the SH are presented in Fig. 5(a). Figure 5(b) illustrates the measured SH power as a function of the pumping power, showing a quadratic relation between the pump and signal. Because the SH is generated from the surface of Si, the normalized SH conversion efficiency is about 5×10^{-10}/W (see Fig. S16 [48]). This result is higher than that obtained from the Si-based qBIC metasurfaces with extremely large Q factors [4]. The measured SH in the real space is shown in Fig. 5(c) by scanning the location of pumping beam. The intensity profile indicates an enhanced field of the Bloch mode in the center of PCS.

Figure 5(d) shows the experimental results of the SH power in supercell PCSs with different R and δ_B, pumped by a laser power of 14.3 mW. Ideally, the valley modes do not generate SH from the Γ-point pump. However, the nanoscale roughness in the fabricated meta-atoms naturally induces spatially variant perturbations that create a momentum channel for SH. The results presented in Fig. 5(e) span different Bloch modes for the wavelength of interest, including qBICs and FMs, via different δ_B. Among them, a maximum SH power enhancement factor of ~340 is achieved between a qBIC ($R = 149$ nm, $\delta_B = 5°$) and a FM ($R = 147$ nm, $\delta_B = 20°$), with a maximum power of

~891 pW. In general, we observe about 2 orders of magnitude SH enhancement as δ_B increases from 0° to 20° [Fig. 5(e)]. These results demonstrate the robust performance of FM in SH generation against parameter changes, in good agreement with the theoretical prediction [48] (Supplemental Material, Sec. S10). Notably, the highest SH from the FMs compared to that from a bared Si film is larger than 10^6 [Fig. 5(e)].

Discussion—In conclusion, we have introduced a supercell PCS featuring paired rotations of triangular meta-atoms, inspired by the structural distortion of natural noncentrosymmetric compounds like HoAgGe, where two types of triangular units rotate oppositely. This paired rotation induces a continuous nearfield vortex dynamic for paired Bloch modes, which maintain a double mode degeneracy at the Γ point due to the supercell's C_3 symmetry. This approach enables flexible tuning of Bloch mode properties, including quality factor, momentum (Brillion-zone folding), spatial symmetry, and nonlinear overlap factor. Different stages of these modes are distinctly defined by unique nearfield vortex distributions. We show an optical analogy of FM within the PCS, presented as degenerate two-down–one-up and two-up–one-down pseudospin vortex textures. These FMs serve as an optimal condition for SH generation by maximizing the $Q\beta$ factor, a mechanism that contrasts with SH generation from qBICs. Geometric frustration has been a powerful paradigm for discovery intriguing physics via asymmetry interactions of various oscillation degrees of freedom. Especially, the coupling between optical modes can be mapped as the interaction between magnetic spins. Alongside its abundant mode degeneracy, geometric frustration also brings forth interesting symmetry properties. This may lead to unusual results in nonlinear light-matter interactions that so far still remains as a rarely explored subject. Our rotational design strategy can be broadly applied, including the creation of larger supercells or the extension from in-plane rotation to out-of-plane tilting, offering a versatile framework for designing supercell photonic crystals with tailored properties and promising applications in nonlinear optics, optical forces, and laser effect. For instance, constructing our supercell PCS with a bulk nonlinear material, such as niobate nitride or gallium arsenide, may offer considerably large SH power from a moderate pump intensity [48] (see Supplemental Material, Sec. S15 for GaAs-based simulation).

Acknowledgments—This work is supported by National Key R&D Program of China (2022YFA1205101), National Science Foundation of China (12274296,12192252, 12474304, 12350403), Shanghai International Cooperation Program for Science and Technology (22520714300), Shanghai Jiao Tong University 2030 Initiative, Beijing Natural Science Foundation (Z240005). B. W. and T. L. are sponsored by the Yangyang Development Fund. The samples were fabricated in the center for advanced electronics materials and devices (AEMD), Shanghai Jiao Tong University.

Data availability—The data supporting this study's findings are available within the Letter.

[1] A. Kodigala, T. Lepetit, Q. Gu, B. Bahari, Y. Fainman, and B. Kanté, Lasing action from photonic bound states in continuum, Nature (London) **541**, 7636 (2017).
[2] Y. G. Sang, J. Y. Lu, Y. H. Ouyang, H. Y. Luan, J. H. Wu, J. Y. Li, and R. M. Ma, Topological polarization singular lasing with highly efficient radiation channel, Nat. Commun. **13**, 6485 (2022).
[3] T. T. H. Do, M. Nonahal, C. Li, V. Valuckas, H. H. Tan, A. I. Kuznetsov, H. S. Nguyen, I. Aharonovich, and S. T. Ha, Room-temperature strong coupling in a single-photon emitter-metasurface system, Nat. Commun. **15**, 2281 (2024).
[4] Z. Liu, Y. Xu, Y. Lin, J. Xiang, T. Feng, Q. Cao, J. Li, S. Lan, and J. Liu, High-Q quasibound states in the continuum for nonlinear metasurfaces, Phys. Rev. Lett. **123**, 253901 (2019).
[5] G. Zograf *et al.*, High-harmonic generation from resonant dielectric metasurfaces empowered by bound states in the continuum, ACS Photonics **9**, 567 (2022).
[6] L. Carletti, S. S. Kruk, A. A. Bogdanov, C. De Angelis, and Y. Kivshar, High-harmonic generation at the nanoscale boosted by bound states in the continuum, Phys. Rev. Res. **1**, 023016 (2019).
[7] A. C. Overvig, S. C. Malek, M. J. Carter, S. Shrestha, and N. Yu, Selection rules for quasibound states in the continuum, Phys. Rev. B **102**, 035434 (2020).
[8] K. Koshelev, S. Lepeshov, M. Liu, A. Bogdanov, and Y. Kivshar, Asymmetric metasurfaces with high-Q resonances governed by bound states in the continuum, Phys. Rev. Lett. **121**, 193903 (2018).
[9] C. F. Doiron, I. Brener, and A. Cerjan, Realizing symmetry-guaranteed pairs of bound states in the continuum in metasurfaces, Nat. Commun. **13**, 7534 (2022).
[10] M. Kang, S. Zhang, M. Xiao, and H. Xu, Merging bound states in the continuum at off-high symmetry points, Phys. Rev. Lett. **126**, 117402 (2021).
[11] W. Wang, Y. K. Srivastava, T. C. Tan, Z. Wang, and R. Singh, Brillouin zone folding driven bound states in the continuum, Nat. Commun. **14**, 2811 (2023).
[12] T. Zhang, K. Dong, J. Li, F. Meng, J. Li, S. Munagavalasa, C. P. Grigoropoulos, J. Wu, and J. Yao, Twisted moiré photonic crystal enabled optical vortex generation through bound states in the continuum, Nat. Commun. **14**, 6014 (2023).
[13] B. Lou, N. Zhao, M. Minkov, C. Guo, M. Orenstein, and S. Fan, Theory for twisted bilayer photonic crystal slabs, Phys. Rev. Lett. **126**, 136101 (2021).
[14] H. Qin, Z. Su, M. Liu, Y. Zeng, M. C. Tang, M. Li, Y. Shi, W. Huang, C. W. Qiu, and Q. Song, Arbitrarily polarized bound states in the continuum with twisted photonic crystal slabs, Light **12**, 66 (2023).

[15] D. Yu, G. Li, L. Wang, D. Leykam, L. Yuan, and X. Chen, Moiré lattice in one-dimensional synthetic frequency dimension, Phys. Rev. Lett. **130**, 143801 (2023).
[16] X. Gao, L. Yang, H. Lin, L. Zhang, J. Li, F. Bo, Z. Wang, and L. Lu, Dirac-vortex topological cavities, Nat. Nanotechnol. **15**, 1012 (2020).
[17] X. R. Mao, Z. K. Shao, H. Y. Luan, S. L. Wang, and R. M. Ma, Magic-angle lasers in nanostructured moiré superlattice, Nat. Nanotechnol. **16**, 1099 (2021).
[18] W. Liu, B. Wang, Y. Zhang, J. Wang, M. Zhao, F. Guan, X. Liu, L. Shi, and J. Zi, Circularly polarized states spawning from bound states in the continuum, Phys. Rev. Lett. **123**, 116104 (2019).
[19] Y. Chen *et al.*, Observation of intrinsic chiral bound states in the continuum, Nature (London) **613**, 474 (2023).
[20] F. Gao, H. Xue, Z. Yang, K. Lai, Y. Yu, X. Lin, Y. Chong, G. Shvets, and B. Zhang, Topologically protected refraction of robust kink states in valley photonic crystals, Nat. Phys. **14**, 140 (2018).
[21] J. Lu, C. Qiu, M. Ke, and Z. Liu, Valley vortex states in sonic crystals, Phys. Rev. Lett. **116**, 093901 (2016).
[22] H. Kwon, D. Sounas, A. Cordaro, A. Polman, and A. Alù, Nonlocal metasurfaces for optical signal processing, Phys. Rev. Lett. **121**, 173004 (2018).
[23] K. Rong *et al.*, Spin-valley Rashba monolayer laser, Nat. Mater. **22**, 1085 (2023).
[24] X. Duan, B. Wang, K. Rong, C. Liu, V. Gorovoy, S. Mukherjee, V. Kleiner, E. Koren, and E. Hasman, Valley-addressable monolayer lasing through spin-controlled Berry phase photonic cavities, Science **381**, 1429 (2023).
[25] A. de Hoogh, A. Opheij, M. Wulf, N. Rotenberg, and L. Kuipers, Harmonics generation by surface plasmon polaritons on single nanowires, ACS Photonics **3**, 1446 (2016).
[26] A. I. Kuznetsov, A. E. Miroshnichenko, M. L. Brongersma, Y. S. Kivshar, and B. Luk'yanchuk, Optically resonant dielectric nanostructures, Science **354**, aag2472 (2016).
[27] C. Fang, Q. Yang, Q. Yuan, L. Gu, X. Gan, Y. Shao, Y. Liu, G. Han, and Y. Hao, Efficient second-harmonic generation from silicon slotted nanocubes with bound states in the continuum, Laser Photonics Rev. **16**, 2100498 (2022).
[28] Z. Liu, J. Wang, B. Chen, Y. Wei, W. Liu, and J. Liu, Giant enhancement of continuous wave second harmonic generation from few-layer GaSe coupled to high-Q quasi bound states in the continuum, Nano Lett. **21**, 7405 (2021).
[29] S. Klimmer, O. Ghaebi, Z. Gan, A. George, A. Turchanin, G. Cerullo, and G. Soavi, All-optical polarization and amplitude modulation of second-harmonic generation in atomically thin semiconductors, Nat. Photonics **15**, 837 (2021).
[30] L. Qu, L. Bai, C. Jin, Q. Liu, W. Wu, B. Gao, J. Li, W. Cai, M. Ren, and J. Xu, Giant second harmonic generation from membrane metasurfaces, Nano Lett. **22**, 9652 (2022).
[31] K. O'Brien, H. Suchowski, J. Rho, A. Salandrino, B. Kante, X. Yin, and X. Zhang, Predicting nonlinear properties of metamaterials from the linear response, Nat. Mater. **14**, 379 (2015).
[32] Z. Lin, X. Liang, M. Lončar, S. G. Johnson, and A. W. Rodriguez, Cavity-enhanced second-harmonic generation via nonlinear-overlap optimization, Optica **3**, 233 (2016).
[33] G. Li, S. Chen, N. Pholchai, B. Reineke, P. W. H. Wong, E. Y. B. Pun, K. W. Cheah, T. Zentgraf, and S. Zhang, Continuous control of the nonlinearity phase for harmonic generations, Nat. Mater. **14**, 607 (2015).
[34] J. Xu, E. Plum, V. Savinov, and N. I. Zheludev, Second harmonic generation in amorphous silicon-on-silica metamaterial, APL Photonics **6**, 036110 (2021).
[35] G. C. Li, D. Lei, M. Qiu, W. Jin, S. Lan, and A. V. Zayats, Light-induced symmetry breaking for enhancing second-harmonic generation from an ultrathin plasmonic nanocavity, Nat. Commun. **12**, 4326 (2021).
[36] L. Carletti, A. Locatelli, D. Neshev, and C. De Angelis, Shaping the radiation pattern of second-harmonic generation from AlGaAs dielectric nanoantennas, ACS Photonics **3**, 1500 (2016).
[37] M. Minkov, D. Gerace, and S. Fan, Doubly resonant $\chi^{(2)}$ nonlinear photonic crystal cavity based on a bound state in the continuum, Optica **6**, 1039 (2019).
[38] R. Sarma, J. Xu, D. de Ceglia, L. Carletti, J. Klem, M. A. Belkin, and I. Brener, Control of second-harmonic generation in all-dielectric intersubband metasurfaces by controlling the polarity of $\chi^{(2)}$, Opt. Express, OE **30**, 34533 (2022).
[39] R. Sarma, J. Xu, D. de Ceglia, L. Carletti, S. Campione, J. Klem, M. B. Sinclair, M. A. Belkin, and I. Brener, An all-dielectric polaritonic metasurface with a giant nonlinear optical response, Nano Lett. **22**, 896 (2022).
[40] S. Stich, J. Mohajan, D. de Ceglia, L. Carletti, H. Jung, N. Karl, I. Brener, A. W. Rodriguez, M. A. Belkin, and R. Sarma, Inverse design of an all-dielectric nonlinear polaritonic metasurface, arXiv:2409.18196.
[41] J. Wang, M. Clementi, M. Minkov, A. Barone, J. F. Carlin, N. Grandjean, D. Gerace, S. Fan, M. Galli, and R. Houdré, Doubly resonant second-harmonic generation of a vortex beam from a bound state in the continuum, Optica **7**, 1126 (2020).
[42] K. Koshelev, S. Kruk, E. Melik-Gaykazyan, J. H. Choi, A. Bogdanov, H. G. Park, and Y. Kivshar, Subwavelength dielectric resonators for nonlinear nanophotonics, Science **367**, 288 (2020).
[43] R. S. Fishman, Phase diagram of a geometrically frustrated triangular-lattice antiferromagnet in a magnetic field, Phys. Rev. Lett. **106**, 037206 (2011).
[44] J. Lu, C. Qiu, L. Ye, X. Fan, M. Ke, F. Zhang, and Z. Liu, Observation of topological valley transport of sound in sonic crystals, Nat. Phys. **13**, 369 (2017).
[45] X. T. He, E. T. Liang, J. J. Yuan, H. Y. Qiu, X. D. Chen, F. L. Zhao, and J. W. Dong, A silicon-on-insulator slab for topological valley transport, Nat. Commun. **10**, 872 (2019).
[46] Y. Yang, Y. Yamagami, X. Yu, P. Pitchappa, J. Webber, B. Zhang, M. Fujita, T. Nagatsuma, and R. Singh, Terahertz topological photonics for on-chip communication, Nat. Photonics **14**, 7 (2020).
[47] K. Zhao, H. Deng, H. Chen, K. A. Ross, V. Petříček, G. Günther, M. Russina, V. Hutanu, and P. Gegenwart, Realization of the kagome spin ice state in a frustrated intermetallic compound, Science **367**, 1218 (2020).
[48] See Supplemental Material at http://link.aps.org/supplemental/10.1103/svcj-vgzw, which includes Refs. [7,37,49], for numerical simulation methods, sample fabrication, experimental setup for spectrum and SHG measurements, symmetry analysis of supercell PCS,

detailed properties of supercell Bloch modes, temporal coupled-mode theory for SHG, and additional SHG simulation using other materials.

[49] A. Rodriguez, M. Soljačić, J. D. Joannopoulos, and S. G. Johnson, $\chi^{(2)}$ and $\chi^{(3)}$ harmonic generation at a critical power in inhomogeneous doubly resonant cavities, Opt. Express **15**, 7303 (2007).

[50] S. Fan, W. Suh, and J. D. Joannopoulos, Temporal coupled-mode theory for the Fano resonance in optical resonators, J. Opt. Soc. Am. A **20**, 569 (2003).